Results in Physics 57 (2024) 107310

Contents lists available at ScienceDirect

Results in Physics

journal homepage: www.elsevier.com/locate/rinp

Electron-positron generation by irradiating various metallic materials with laser-accelerated electrons

Hyeong-il Kim [a,b], Youhwan Noh [a,b], Jaehyun Song [a,b], Seongmin Lee [a,b], Junho Won [a,b], Chiwan Song [a,b], Leejin Bae [c], Chang-Mo Ryu [d], Chang Hee Nam [a,b], Woosuk Bang [a,b,*]

[a] Department of Physics and Photon Science, GIST, Gwangju 61005, South Korea
[b] Center for Relativistic Laser Science, Institute for Basic Science, Gwangju 61005, South Korea
[c] Advanced Photonics Research Institute, GIST, Gwangju 61005, South Korea
[d] Department of Physics, POSTECH, Pohang 37673, South Korea

ARTICLE INFO

Keywords:
Electron-positron pair production
Laser wakefield acceleration
GEANT4 simulations
Laser-plasma physics

ABSTRACT

We examined electron–positron pair production in solid iron, zinc, tungsten, and lead targets irradiated by a laser-accelerated electron beam generated with a 100 TW laser. These targets were assessed at the target thickness of 0.5, 1.25, and 2.0 radiation lengths for each material. Using a 0.75-T-magnetic spectrometer, we measured the electron and positron yields and spectra, producing 3×10^8 positrons per shot with a peak leptonic density of 4×10^{12} cm^{-3}. These experimental results agree very well with Monte Carlo simulations conducted with the simulation code Geant4. Importantly, our findings show that normalizing the target thickness to each material's radiation length results in consistent electron and positron yields across the materials, effectively reducing discrepancies due to material differences.

Introduction

Relativistic electron–positron pair plasmas are essential for understanding numerous astrophysical phenomena. These plasmas play a significant role in the magnetospheres of pulsars [1,2], black holes [3], quasars [4], accretion disks in close binary systems [5,6], relativistic jets originating from active galactic nuclei [7–9], and gamma-ray bursts [10]. Furthermore, positron beams have been used for non-invasive material inspection using positron annihilation spectroscopy (PAS) [11].

With the emergence of the chirped pulse amplification technique [12], the laser intensity has surged dramatically, making it feasible to use high-power lasers for positron generation [13–23]. Two distinct methods have been developed for laser-driven positron creation: the 'direct laser-solid interaction' method, in which solid targets are directly irradiated with lasers [13–17], and another method involving the irradiation of targets with relativistic electron beams [18–23] generated by laser wakefield acceleration (LWFA) [24]. In the direct laser-solid interaction approach, hot electrons are produced when the laser directly irradiates the solid. As the electrons traverse materials, they emit bremsstrahlung photons while losing kinetic energy. When these photons possess energies exceeding 1.02 MeV, they can be absorbed in the nuclear field, producing electron–positron pairs [25,26]. The LWFA-based method employs the same positron generation mechanism; however, it uses bremsstrahlung photons produced by LWFA electrons rather than those emitted from hot electrons in direct laser-solid interactions.

Although the direct laser-solid interaction method is much simpler to implement and produces more positrons than the LWFA approach [27], the LWFA-based method is considered much more advantageous when the quality of the generated positron beam is important. LWFA electrons can produce high-energy (exceeding hundreds of MeVs), low-divergence, and nearly charge-neutral electron–positron beams [21,28]. Such properties are particularly valuable in laboratory astrophysics experiments for creating controlled electron–positron plasmas [29,30]. Additionally, for applications in PAS, these energetic positrons can detect deeper material defects owing to their higher kinetic energy compared with conventional sources such as the sodium-22 isotope, which only emits positrons at energies of a few hundred keV [31].

Sarri *et al.* [19] and Xu *et al.* [23] previously reported on generating electron–positron beams using LWFA electron beams. Sarri *et al.* investigated a range of materials, including copper, tin, tantalum, and lead, focusing on a specific energy range from 90 MeV to 140 MeV for positron detection. Similarly, Xu *et al.* examined the positron energy spectra of

* Corresponding author at: Department of Physics and Photon Science, GIST, Gwangju 61005, South Korea.
E-mail address: wbang@gist.ac.kr (W. Bang).

https://doi.org/10.1016/j.rinp.2023.107310
Received 22 September 2023; Received in revised form 25 December 2023; Accepted 26 December 2023
Available online 4 January 2024

copper and lead. However, their findings revealed some discrepancies between the observed yields and those predicted by simulations, which underscore the need for further research.

In this study, we used LWFA electrons to generate electron–positron beams, employing the 100 TW laser at the Center for Relativistic Laser Science [32]. We compared the electron–positron beam spectra of four target materials: two low-Z solids (iron and zinc) and two high-Z solids (tungsten and lead). We successfully measured electron and positron spectra ranging from 4 MeV to over 300 MeV, using a pair spectrometer equipped with a 0.75 T magnet. To address the variations in material properties, we normalized the target thicknesses using the radiation length L_R, corresponding to the average distance that high-energy electrons travel before their energy is reduced by $1/e$ due to bremsstrahlung. By adopting L_R as a normalized unit of thickness, we effectively mitigated the dependence on the atomic number of the material. Our findings revealed that electron and positron yields were consistent across various materials when adjusted to similar thicknesses in L_R for each material. Our experimental results agreed well with Monte Carlo simulations using Geant4 [33].

Results

Fig. 1 shows a schematic of the experimental setup. The laser beam we used had a central wavelength of 800 nm, a pulse duration of 27 fs (full width at half maximum, FWHM), and an energy of 2.1 J (after compression). The laser beam was focused using a $f/23$ spherical mirror, resulting in a spot size of 23 μm (FWHM). This arrangement led to a peak laser intensity of 3.6×10^{18} W/cm^2 at the focus. We focused the laser beam on a gas jet emitted from a cylindrical nozzle with a 4 mm diameter and a backing pressure of 28 bar. The gas density, measured using a Phasics SID4-HR wavefront sensor [34], was on the order of 3×10^{18} cm^{-3} at a height of 3.5 mm from the nozzle. This setup allowed us to generate LWFA electrons. The charge of the electron beam was enhanced by employing a mixed gas of 97 % helium and 3 % nitrogen [35]. A Kodak Lanex scintillating screen was positioned between the gas jet and the solid target. This screen monitors both the beam profile and charge of the LWFA electron beam. The Lanex screen was cross-calibrated with a Fujifilm BAS-MS imaging plate (IP) and used for charge measurements [36].

For the electron–positron pair production target, we used twelve solids composed of four different materials (iron, zinc, tungsten, and lead) with three given thicknesses (see Table 1). We used L_R as a unit of thickness for the targets composed of different materials. The radiation length of each target was approximated using the equation proposed by Tsai [37]. These targets were positioned behind the Lanex screen and mounted on a motorized stage to facilitate easy interchangeability without breaking the vacuum.

Table 1
Material and thickness of each solid target.

Materials	L_R for each material (mm)	Target thickness (mm)	Normalized thickness (L_R)
Iron	17.57	8.71	0.50
		21.78	1.24
		34.84	1.98
Zinc	17.42	8.71	0.50
		21.78	1.25
		34.84	2.00
Tungsten	3.50	1.87	0.53
		4.25	1.21
		7.01	2.00
Lead	5.61	2.75	0.49
		7.00	1.25
		11.36	2.02

The incident LWFA electron beam on the target exhibited an average charge of 167 ± 38 pC, accompanied by an FWHM divergence of approximately 3 mrad [see Fig. 2(a)]. Fig. 2(b) shows the 20-shot cumulative energy spectra of the electrons, as measured by a pair

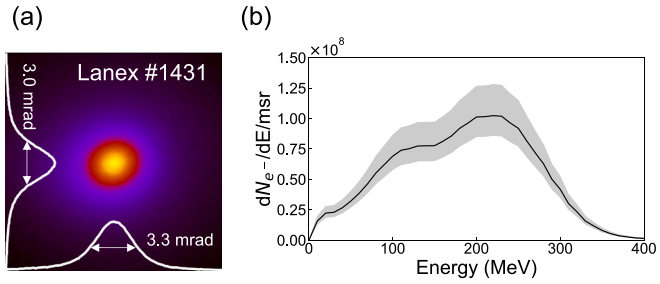

Fig. 2. Divergence and energy spectrum of LWFA electron beam. (a): Lanex screen image captured by CCD, illustrating the x and y-axis divergence (FWHM) of the LWFA electron beam. (b): A 20-shot cumulative LWFA electron spectrum recorded on the pair spectrometer without a solid target. Error bars represent the uncertainty from converting the PSL signal on the IPs to electron counts.

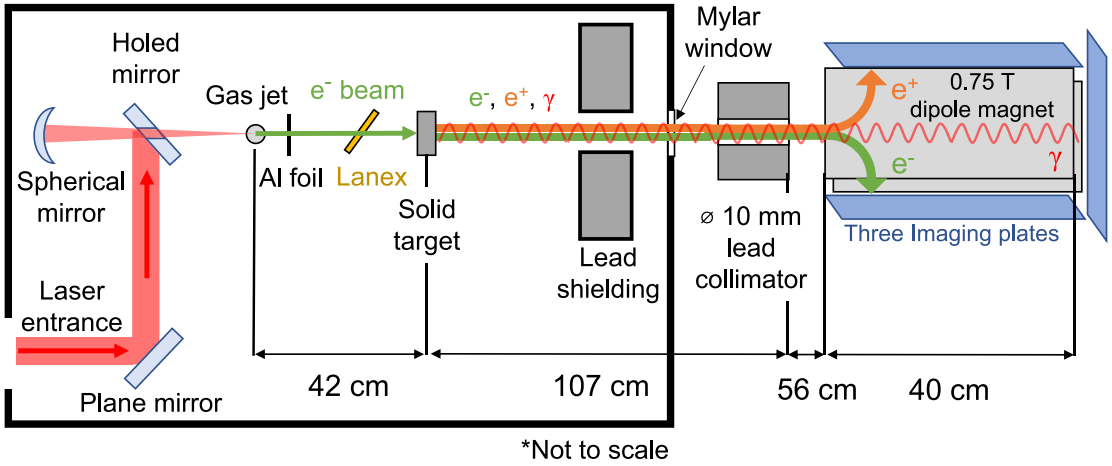

Fig. 1. Schematic of the experimental setup. Electrons are accelerated from a gas jet (97 % He and 3 % N_2). A 0.4-mm-thick aluminum foil blocks the transmitted laser light, allowing only the electron beam to pass. The direction and charge of the electron beam are determined using a Lanex scintillating screen. Solid targets of various materials and thicknesses serve as converters of electron–positron pair production. Particles leave the chamber through a 200-μm-thick mylar window. A 20-cm-long lead collimator with a 10 mm diameter cylindrical hole makes a 3.3 mrad acceptance angle. A 0.75 T and 40-cm-long dipole magnet functions as the charged particle spectrometer. Imaging plates on three sides of the magnet detect electrons and positrons with energies above 4 MeV.

spectrometer (see Appendix A). As a simultaneous measurement of the energy spectrum during the irradiation of the solid target was not feasible, this spectrum was independently measured without the solid target. The energy spectrum peaked at approximately 230 MeV, with some electrons possessing an energy over 300 MeV.

Fig. 3 displays typical electron–positron spectra recorded on the three IPs attached to the pair spectrometer. These are 20-shot accumulated IP images with a tungsten target with a thickness of 1.21 L_R (4.25 mm). The experimental setup involved positioning three IPs to cover the three sides of the magnet, as illustrated in Fig. 1(b).

The front IP was positioned at the end of the magnet [see Fig. 3(a)], normal to the beam axis. Because of the bending effect of the magnetic field on the paths of the incoming charged particles, positrons were detected on the left side of the front IP, whereas electrons were detected on the right side. The front IP detects charged particles with energies exceeding 170 MeV. Notably, the image in Fig. 3(a) displays collimated bremsstrahlung photons at the center of the IP, indicating a high level of particle collimation by lead. Similarly, incoming electrons and positrons directed towards the pair spectrometer, within an energy range of 4–289 MeV, headed to the IPs on each side of the magnet [see Fig. 3(b), 3 (c)]. For quantitative analysis, we selected the central portion of the IP with a height of 16.4 mm, corresponding to the acceptance angle of 3.3 mrad at the front IP.

Despite the implementation of effective radiation shielding in the setup, it is important to note that secondary radiation can still be detected on the IPs. We performed Geant4 simulations of our experimental setup to assess the effects of secondary radiation. The results revealed that approximately 30 % of the total photostimulated luminescence (PSL) signal detected at the positron-side IP originated from the secondary electrons and photons [solid red line in Fig. 3(d)]. These particles are distributed throughout the IP. Similarly, the simulation showed that approximately 2 % of the total PSL in the electron-side IP was composed of secondary particles. Considering the background contribution from secondary radiation, we corrected the PSL from the raw data to ensure accuracy.

Fig. 4 shows the electron and the positron spectra obtained from twelve distinct solid targets, segmented by material and thickness. Measured and simulated results (using Geant4) are also presented. One of the most striking observations was the similarity in the electron–positron spectra across different materials at the same thicknesses in L_R. This similarity in the electron–positron spectra, regardless of the material type, reinforces the efficacy of employing L_R as a normalized unit of measure.

Across all the tested targets, the electron counts consistently surpassed the number of positrons in every energy range. This dominance of electrons was anticipated, considering that our experimental setup employed an electron beam as the primary driver for pair production. A notable fraction of high-energy electrons can traverse solid targets, resulting in their simultaneous detection alongside pair-produced particles.

The disparity between the electrons and positrons was reduced for targets with increased thickness. Our experiment focused on a tightly collimated beam characterized by a narrow acceptance angle of 3.3 mrad. As the incident electrons moved through the target, they underwent scattering, an effect that is amplified with thicker targets. This scattering affects the incoming electrons and newly produced electron–positron pairs, resulting in decreased yields for thicker targets. However, the inherent angular distributions of the pair-produced

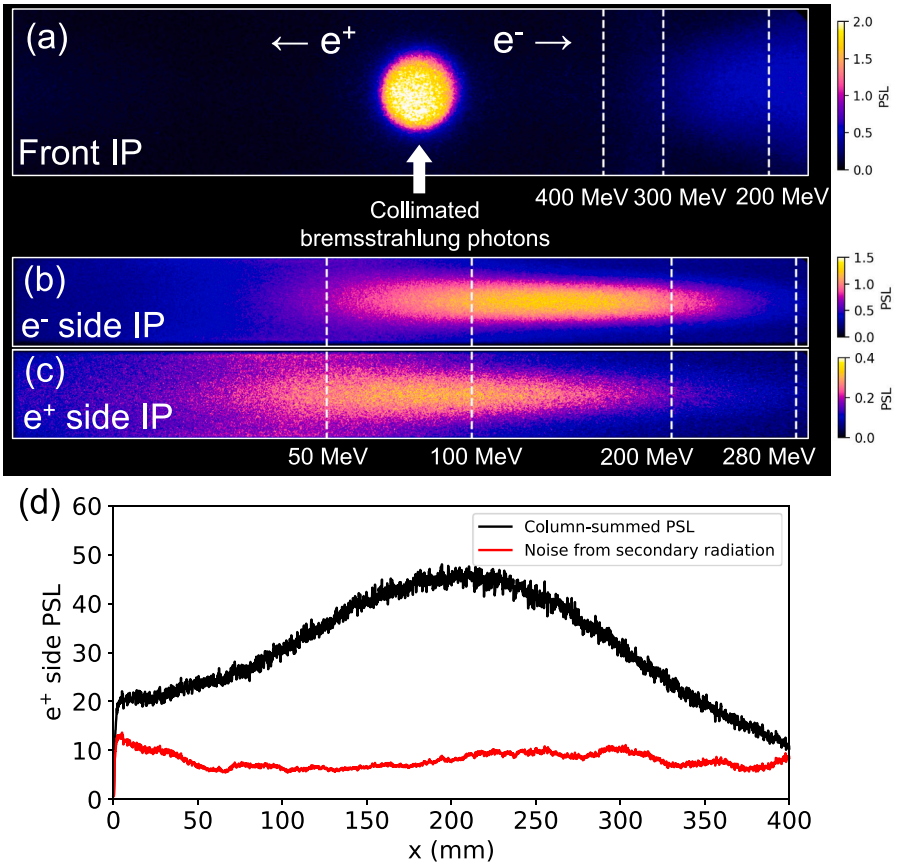

Fig. 3. Typical PSL signal from the three IPs at the pair spectrometer. Image of the 20-shot accumulated PSL signal with a 4.25 mm tungsten target. (a): IP positioned at the end of the magnet adjacent to the beam axis. (b): Image from the IP at the electron side (electron-side IP). (c): Image from the IP at the positron side (positron-side IP). (d): Column-summed PSL values from the positron-side IP. The solid red line denotes the background noise as predicted by Geant4. (For interpretation of the references to colour in this figure legend, the reader is referred to the web version of this article.)

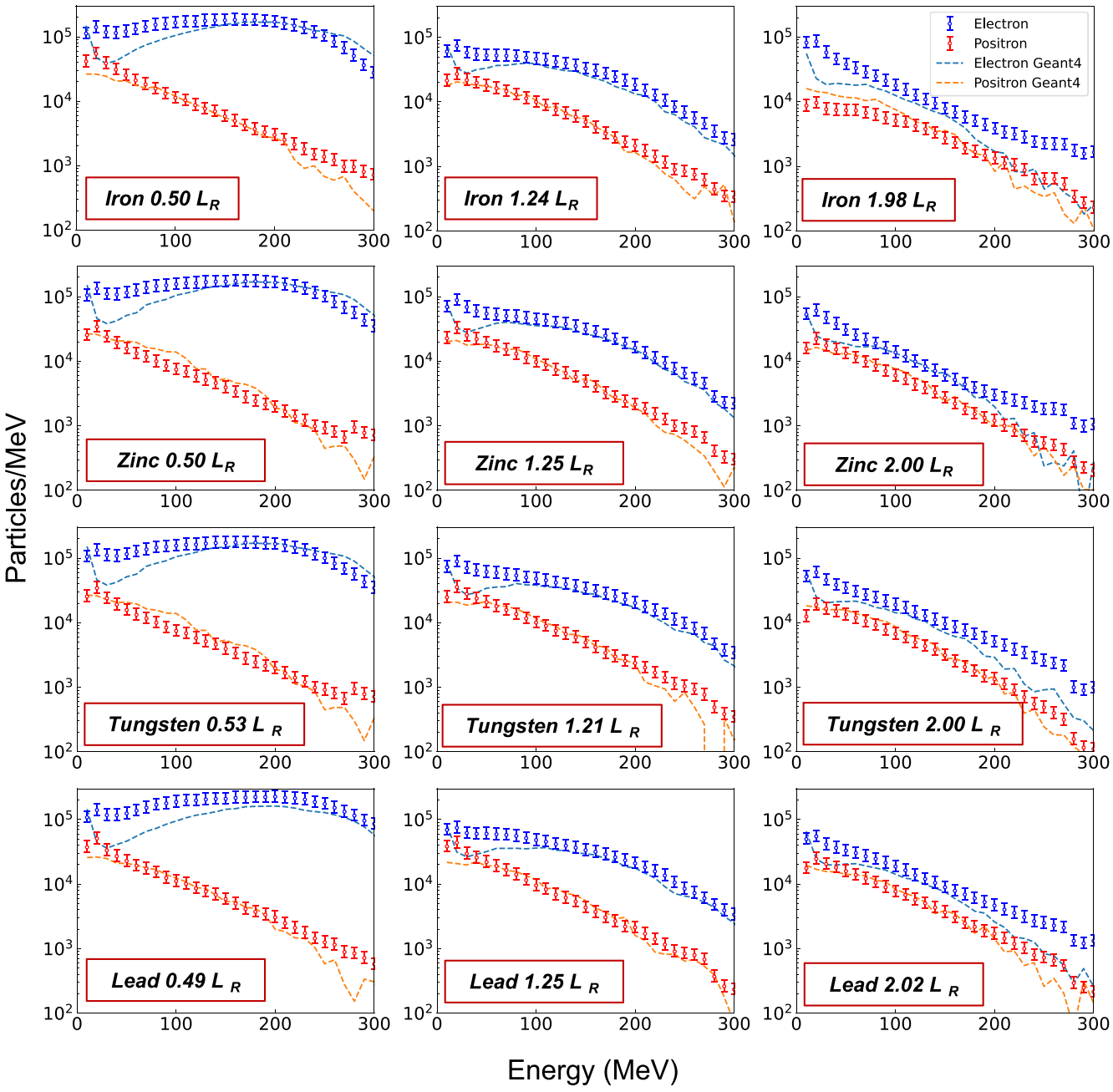

Fig. 4. Electron and positron energy spectra normalized for each target. Blue and red markers with error bars represent the 20-shot accumulated spectra for electrons and positrons, respectively. These spectra are averaged over every 10 MeV range and normalized to the average charge of the accumulated incident electron. Error bars indicate uncertainties arising from the PSL response of the IP (see Appendix B). The blue and orange dashed lines illustrate the electron and positron spectra from the simulation with Geant4.

electrons and positrons are symmetric, implying that they have equivalent yields. Therefore, as the target thickness increases, the influence of the incident electron beam decreases, causing the yields and spectra of the electrons and positrons to become more similar.

The positron yields from our experiments were in good agreement with the simulation predictions. However, the observed electron yields surpassed the simulated results for most targets. A potential reason for this discrepancy could be that secondary radiation sources were not considered in the simulations. For example, supporting steel structures for magnets can introduce additional radiation. Because of the higher yield of electrons compared with that of positrons, these secondary sources are likely to significantly influence the electron-side IP.

The normalized yields of electrons and positrons per shot from the twelve solid targets are depicted in Fig. 5. The colored markers with error bars denote the experimental data obtained from various target materials: blue triangles for iron, black squares for zinc, orange circles for tungsten, and red diamonds for lead. The yields were normalized to the average charge of the incident electron beam for each shot. The simulation results are shown using various line styles after polynomial fitting. Consistent with the earlier findings shown in Fig. 4, employing L_R as a normalized unit for thickness effectively mitigated material-specific discrepancies. Regardless of the intrinsic properties of the selected target material, the yield exhibited small fluctuations, reinforcing the robustness of the normalization approach. Notably, at approximately 1.25 L_R,

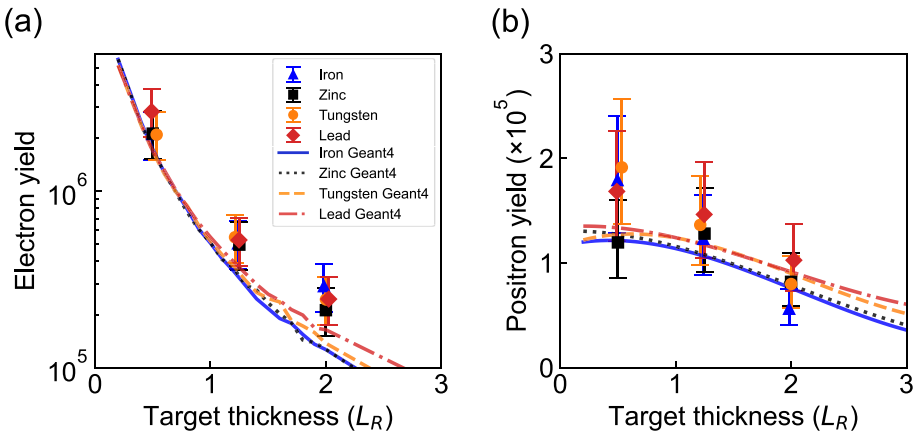

Fig. 5. Normalized electron and positron yield as a function of target thickness. (a): Normalized electron yield per shot as a function of target thickness. (b): Normalized positron yield per shot as a function of target thickness. Colored markers with error bars represent the experimental data, while the simulation results are shown using various line styles (solid, dotted, dashed, and dash-dot) for each target material.

the deviation in positron yield was about 7 %, which is significantly less than the estimated experimental yield error of 23 %.

In our measurements, the presence of a narrow lead collimator affected the detected electron and positron yield. For example, simulations without a collimator indicate that the total number of positrons exiting the back surface of the target increases with the thickness, peaking at approximately 2 L_R [30]. In general, the divergence angle of the emitted positrons broadened owing to the scattering within the target. Consequently, as the target thickness increased, the experimental data and our simulation results consistently indicated a decline in the measured positron yields on the IPs.

The fitted simulation results of electron and positron yields for iron, zinc, tungsten, and lead targets using Geant4 are represented by different line styles: solid, dotted, dashed, and dash-dot, respectively. Geant4 simulations showed a modest variance in maximum positron yield for each material across the four target materials, with a deviation of approximately 6 % between the highest and the lowest maximum yields. In our simulations, even when the thickness was normalized using L_R, high-Z materials tended to generate slightly more positrons than their low-Z counterparts. This can be attributed to how electrons and photons dissipate energy within materials, particularly in the energy range of approximately 10 MeV. For electron energies exceeding several hundred MeV, the dominant loss mechanism is the bremsstrahlung process, with losses proportional to Z^2. Setting the target thickness based on L_R compensates for this material dependence because L_R scales inversely with Z^2. In the lower electron energy ranges, excitation and ionization of atoms from collisions play a significant role in low-Z solids, leading to diminished bremsstrahlung photon yields [38]. Furthermore, despite normalizing the thickness based on L_R, low-Z materials exhibit a higher probability of Compton scattering than pair production when exposed to photons in the few-MeV range [39]. Consequently, low-Z materials produce fewer positrons than their high-Z counterparts.

Given that we measured the electron–positron beam with the pair spectrometer positioned behind a narrow lead collimator, we anticipate that the total number of electrons and positrons at the back surface of the target is significantly higher than what we measured. For lead targets with a thickness equivalent to 1.25 L_R, Geant4 simulations estimated the number of positrons at the rear surface of the target to be on the order of $3.2\ (\pm 0.7) \times 10^8$ per shot. This count was approximately 25 times higher than the measured yield. The density of the leptonic beam can be determined using these data. Considering that the duration of the pair-particle beam is approximately 30 fs [40] and that the simulated beam diameter at the target surface is 6.6 mm (in $1/e^2$ width), the estimated leptonic density near the back surface of the target was calculated to be $4.6\ (\pm 0.9) \times 10^{12}$ cm^{-3}. This gives a relativistic skin depth, given by $c\sqrt{\gamma m \varepsilon_0 / ne^2}$, of 17.2 mm for a median leptonic particle's energy of 24 MeV, which is approximately 2.6 times larger than the diameter of the beam. While the transverse size of the beam being smaller than the relativistic skin depth makes it challenging to categorize the beam as plasma, further optimizations in future experiments could help approach the ideal conditions [30].

Charge neutrality, defined as $N_{e+} / (N_{e+} + N_{e-})$, is crucial in creating the electron–positron pair plasma. Fig. 6 shows the charge neutrality of electron–positron beams at the pair spectrometer, each with energies exceeding 100 MeV and within a 3.3 mrad angle, as measured by the pair spectrometer for various targets. Given the notable differences between our experimental results and the Geant4 simulations in the low-energy domain, as illustrated in Fig. 4, we limited our charge neutrality analysis to electron–positron beams with energies exceeding 100 MeV. The overarching trend from our experimental data is consistent: charge neutrality increases as target thickness grows. Notably, for targets normalized to a thickness of 1.25 L_R, the deviation was less than 7 %. This confirms the efficacy of using L_R as the characteristic length, resulting in comparable charge neutrality across different materials.

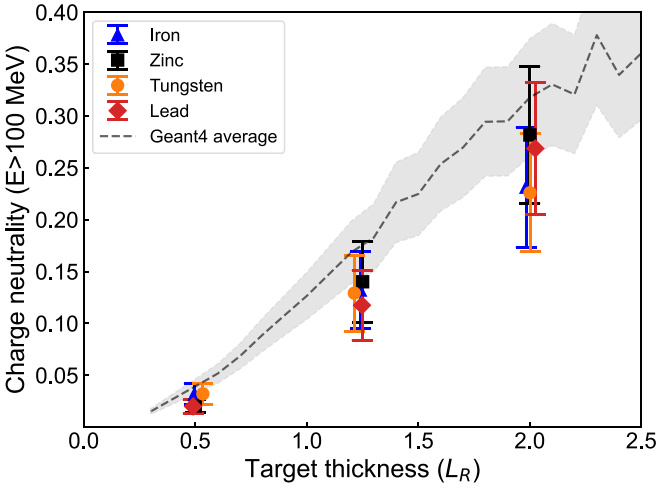

Fig. 6. Measured charge neutrality of the electron–positron beam for twelve targets. Colored markers represent the charge neutrality for leptons with energies above 100 MeV for iron, zinc, tungsten, and lead. The error bars indicate an approximate 28% uncertainty, primarily stemming from the calculations of the electron and positron yields. The dashed grey line depicts the averaged Geant4 simulation results across the four materials. Uncertainties of the simulation results (shaded area) arose from fluctuations in the energy spectrum and directionality of the incident electron beam.

In Fig. 6, the dashed grey line represents the average charge neutrality at the pair spectrometer, from our Geant4 simulations across the four tested materials. These simulations indicated a consistent charge neutrality with a minor deviation of about 3 %. The shaded area in Fig. 6 shows the uncertainties introduced by variations in the pointing and energy of the incident electron beam. The Geant4 simulations presented slightly elevated results relative to our experimental findings. However, it is important to highlight that both simulation and experimental data demonstrate similar trends, particularly in the increasing neutrality as target thickness grows. While simulations may not capture all intricacies of actual experimental conditions, such as the influence of secondary radiation sources, minor deviations in absolute values are anticipated.

Discussion

We analyzed the collimated electron–positron yields and energy spectra from different target materials. Our findings emphasize that using L_R as a normalized unit for target thickness effectively minimizes the variability in electron–positron generation, irrespective of the material type.

The generation of electron–positron plasma depends on two pivotal criteria: the beam should maintain quasi-neutrality, and its length scale should exceed the plasma skin depth. As presented in Fig. 6, our data indicate that the charge neutrality improves with increasing target thickness. However, the leptonic particle density should be increased beyond our current results to achieve a smaller plasma skin depth. Recognizing that a greater target thickness reduces particle density owing to increased divergence, we advocate the use of a higher charge or more energetic electron beam for pair-plasma production.

A detailed simulation by Song *et al.* [30] on electron–positron pair plasma conditions, contingent upon the energy of the electron beam, demonstrated that charge neutrality can exceed 0.4 for a thickness of 2 L_R lead targets with a 2 GeV electron beam. These results align with our discussion emphasizing the importance of high-energy electron beams for effective plasma generation. This finding holds promise for pioneering experiments, particularly those employing multi-GeV LWFA electron beams. Such methodologies enable the generation of electron–positron plasmas in laboratories, potentially catering to astrophysical applications.

A recent experiment by Audet *et al.* [41] used two dipole magnets: one to separate positrons from the electron–positron beam and the other for positron collimation. Drawing inspiration from this approach, integrating an additional magnet specifically for positron collimation into setups such as ours can be a valuable future enhancement. Such an addition would generate a positron beam with a specific energy range, which is particularly beneficial for applications such as PAS, which requires a high-energy and short-duration positron beam.

Conclusion

We used LWFA electrons to produce electron–positron beams across low-Z (iron, zinc) and high-Z (tungsten, lead) materials on a 100 TW laser facility. By normalizing the target thickness using L_R, we effectively reduced material-dependent variability, observing consistent electron–positron yields across various materials. Our spectral analyses, conducted with a 0.75-T-dipole magnet, showed a collimated yield of approximately 10^5 positrons per shot, corresponding to 3×10^8 positrons at the back surface of the target with a peak density of 4×10^{12} cm^{-3}. Notably, the electron and positron yields for the targets normalized in L_R remained consistent, with deviations less than 7 %. These experimental findings confirm that L_R can be regarded as the characteristic length scale in pair production. The electron–positron beams produced in our experiment present potential applications in laboratory astrophysics and PAS.

CRediT authorship contribution statement

Hyeong-il Kim: Writing – review & editing, Writing – original draft, Visualization, Validation, Software, Methodology, Investigation, Formal analysis, Conceptualization. **Youhwan Noh:** Writing – review & editing, Validation, Software, Methodology, Investigation, Conceptualization. **Jaehyun Song:** Writing – review & editing, Methodology, Investigation. **Seongmin Lee:** Writing – review & editing, Methodology, Investigation. **Junho Won:** Writing – review & editing, Methodology, Investigation. **Chiwan Song:** Writing – review & editing, Investigation. **Leejin Bae:** Writing – review & editing, Methodology, Conceptualization. **Chang-Mo Ryu:** Writing – review & editing, Project administration, Conceptualization. **Chang Hee Nam:** Conceptualization, Project administration, Writing – review & editing. **Woosuk Bang:** Writing – review & editing, Supervision, Project administration, Conceptualization.

Declaration of competing interest

The authors declare that they have no known competing financial interests or personal relationships that could have appeared to influence the work reported in this paper.

Data availability

Data will be made available on request.

Acknowledgments

This work was supported by the National Research Foundation of Korea (NRF) grant funded by the Korea government (MSIT) (No. 2023R1A2C1002912) and by the Institute for Basic Science under IBS-R012-D1.

Appendix A. . Pair spectrometer

The magnetic spectrometer used in the experiment consisted of a 40 cm-long dipole NdFeB magnets with a 4 cm gap between the poles. The peak magnetic field strength of the magnet was measured to be 0.75 T. As the charged particles passed through the magnet, their paths were bent, resulting in a spatial distribution of particles at the side and front of the magnet. We numerically calculated the path of the charged particles entering the magnet using a measured magnetic field. For charged particles that follow the beam path, the pair spectrometer could detect particles with energies ranging from 4 to 289 MeV on the side of the magnet and particles with energies greater than 170 MeV on the front side of the magnet.

Appendix B. . Imaging plate (IP)

As high-energy electrons, positrons, or photons traverse the IP, they interact with the phosphor layer, resulting in electron excitation and subsequent transition to metastable states within the IP [42,43]. We employed a GE Amersham Typhoon scanner [44] to recombine these electrons and measure the emitted light from the IPs. This emission is referred to as PSL. It is important to note that the particle type, energy, and incident angle influence the PSL response of the IPs. We adopted the PSL response curves for electrons and photons from previous studies by Boutoux *et al.* [45,46]. Considering the similar fractional energy losses exhibited by both electrons and positrons in the relativistic energy region [47,48], we assumed that the PSL sensitivity of positrons was comparable to that of electrons.

Appendix C. . Geant4 simulation

We employed Geant4 [33] to simulate the experimental setup. A built-in QGSP-BERT physics model was used for the electromagnetic

cascade. The simulation encompassed elements including a solid target, mylar, acrylic windows, lead collimator, and pair spectrometer. The initial electron beam was directed toward the center of the target, with the average divergence from the 20-shot accumulated electron beam (7 mrad). The energy spectrum shown in Fig. 2 served as the spectral shape of the electron beam, and each target received an irradiation of 3 $\times$ 10^7 electrons in the simulation. We collected the positions and energies of the electrons, positrons, and photons at various locations: the target surface, the entrance of the pair spectrometer, and three IPs.

References

[1] Ruderman MA, Sutherland PG. Theory of pulsars: polar gaps, sparks, and coherent microwave radiation. Astrophys J 1975;196:51.
[2] Becker W. Neutron stars and pulsars. Berlin Heidelberg: Springer; 2009.
[3] Hirotani K, Okamoto I. Pair Plasma Production in a Force-free Magnetosphere around a Supermassive Black Hole. Astrophys J 1998;497:563.
[4] Wardle JFC, Homan DC, Ojha R, Roberts DH. Electron–positron jets associated with the quasar 3C279. Nature 1998;395:457.
[5] Takahara F, Kusunose M. Electron-positron pair production in a hot accretion plasma around a massive black hole. Prog Theor Phys 1985;73:1390.
[6] Rose WK. Advanced Stellar Astrophysics. Cambridge University Press; 1998.
[7] Begelman MC, Blandford RD, Rees MJ. Theory of extragalactic radio sources. Rev Mod Phys 1984;56:255.
[8] Peacock JA, Press CU. Cosmological Physics. Cambridge University Press; 1999.
[9] Larrabee DA, Lovelace RVE, Romanova MM. Lepton Acceleration by Relativistic Collisionless Magnetic Reconnection. Astrophys J 2003;586:72.
[10] Piran T. The physics of gamma-ray bursts. Rev Mod Phys 2005;76:1143.
[11] Krause-Rehberg R, Leipner HS. Positron Annihilation in Semiconductors: Defect Studies. Springer; 1999.
[12] Strickland D, Mourou G. Compression of amplified chirped optical pulses. Opt Commun 1985;56:219.
[13] Cowan TE, et al. High energy electrons, nuclear phenomena and heating in petawatt laser-solid experiments. Laser Part Beams 1999;17:773.
[14] Gahn C, et al. Generating positrons with femtosecond-laser pulses. Appl Phys Lett 2000;77:2662.
[15] Chen H, et al. Making relativistic positrons using ultraintense short pulse lasers. Phys Plasmas 2009;16:122702.
[16] Chen H, et al. Magnetic collimation of relativistic positrons and electrons from high intensity laser–matter interactions. Phys Plasmas 2014;21:040703.
[17] Liang E, et al. High e+/e− Ratio Dense Pair Creation with 1021W.cm−2 Laser Irradiating Solid Targets. Sci Rep 2015;5:13968.
[18] Sarri G, et al. Laser-driven generation of collimated ultra-relativistic positron beams. Plasma Phys Contr F 2013;55:124017.
[19] Sarri G, et al. Table-Top Laser-Based Source of Femtosecond, Collimated, Ultrarelativistic Positron Beams. Phys Rev Lett 2013;110:255002.
[20] Schumaker W, et al. Measurements of high-energy radiation generation from laser-wakefield accelerated electron beams. Phys Plasmas 2014;21:056704.
[21] Sarri G, et al. Generation of neutral and high-density electron–positron pair plasmas in the laboratory. Nat Commun 2015;6:6747.
[22] Sarri G, et al. Spectral and spatial characterisation of laser-driven positron beams. Plasma Phys Contr F 2016;59:014015.
[23] Xu T, et al. Ultrashort megaelectronvolt positron beam generation based on laser-accelerated electrons. Phys Plasmas 2016;23:033109.
[24] Tajima T, Dawson JM. Laser Electron Accelerator. Phys Rev Lett 1979;43:267.
[25] H. Bethe, W. Heitler, and P. A. M. Dirac, *On the stopping of fast particles and on the creation of positive electrons*, Proceedings of the Royal Society of London. Series A, Containing Papers of a Mathematical and Physical Character **146**, 83 (1934).
[26] K.I. Nakashima and H. Takabe, *Numerical study of pair creation by ultraintense lasers*, Physics of Plasmas **9**, 1505 (2002).
[27] Alejo A, Samarin GM, Warwick JR, Sarri G. Laser-Wakefield Electron Beams as Drivers of High-Quality Positron Beams and Inverse-Compton-Scattered Photon Beams. Front Phys 2019;7.
[28] Noh Y, et al. Charge-neutral, GeV-scale electron-positron pair beams produced using bremsstrahlung gamma rays. Commun Phys 2024;7. https://doi.org/10.1038/s42005-024-01527-7.
[29] Warwick J, et al. Experimental Observation of a Current-Driven Instability in a Neutral Electron-Positron Beam. Phys Rev Lett 2017;119:185002.
[30] Song H, et al. Characterization of relativistic electron–positron beams produced with laser-accelerated GeV electrons. Sci Rep 2023;13:310.
[31] Čížek J. Characterization of lattice defects in metallic materials by positron annihilation spectroscopy: A review. J Mater Sci Technol 2018;34:577.
[32] Sung JH, et al. 5-Hz, 150-TW Ti:sapphire Laser with High Spatiotemporal Quality. J Korean Phys Soc 2020;77:223.
[33] Allison J, et al. Recent developments in Geant4. Nucl Instrum Methods Phys Res, Sect A 2016;835:186.
[34] Bon P, Maucort G, Wattellier B, Monneret S. Quadriwave lateral shearing interferometry for quantitative phase microscopy of living cells. Opt Express 2009;17:13080–94.
[35] Pak A, et al. Injection and Trapping of Tunnel-Ionized Electrons into Laser-Produced Wakes. Phys Rev Lett 2010;104:025003.
[36] Tanaka KA, et al. Calibration of imaging plate for high energy electron spectrometer. Rev Sci Instrum 2004;76:013507.
[37] Tsai Y-S. Pair production and bremsstrahlung of charged leptons. Rev Mod Phys 1974;46:815.
[38] Berger, M.J., Coursey, J.S., Zucker, M.A., and Chang, J. (2005), ESTAR, PSTAR, and ASTAR: Computer Programs for Calculating Stopping-Power and Range Tables for Electrons, Protons, and Helium Ions (version 1.2.3). [Online] Available: http://physics.nist.gov/Star [2023, December 24]. National Institute of Standards and Technology, Gaithersburg, MD.
[39] Berger MJ, Hubbell JH, Seltzer SM, Chang J, Coursey JS, Sukumar R, et al. December 24]. Gaithersburg, MD: National Institute of Standards and Technology; 2023.
[40] Mangles SPD, et al. Laser-Wakefield Acceleration of Monoenergetic Electron Beams in the First Plasma-Wave Period. Phys Rev Lett 2006;96:215001.
[41] T. L. Audet *et al.*, *Ultrashort, MeV-scale laser-plasma positron source for positron annihilation lifetime spectroscopy*, Physical Review Accelerators and Beams **24**, 073402 (2021).
[42] Y. Tateno, T. Iinuma, and M. Takano, *Computed Radiography* (Springer Japan, 1987).
[43] Won J, et al. Monte Carlo Study of Imaging Plate Response to Laser-Driven Aluminum Ion Beams. Appl Sci 2021;11:820.
[44] Kojima S, et al. Absolute response of a Fuji BAS-TR imaging plate to low-energy protons (<0.2 MeV) and carbon ions (<1 MeV). Rev Sci Instrum 2021;92:033306.
[45] Boutoux G, et al. Study of imaging plate detector sensitivity to 5–18 MeV electrons. Rev Sci Instrum 2015;86:113304.
[46] Boutoux G, et al. Validation of modelled imaging plates sensitivity to 1–100 keV x-rays and spatial resolution characterisation for diagnostics for the "PETawatt Aquitaine Laser". Rev Sci Instrum 2016;87:043108.
[47] G. Particle Data *et al.*, *Review of Particle Physics*, Physical Review D **98**, 030001 (2018).
[48] Messel H, Crawford DF. Electron–photon Shower Distribution Function: Tables for Lead, Copper, and Air Absorbers. Pergamon Press; 1970.